Article

Journal of
Nanoscience and Nanotechnology
Vol. 18, 4243–4247, 2018
www.aspbs.com/jnn

Photodetector Based on Multilayer $SnSe_2$ Field Effect Transistor

Moonshik Kang[1,2], Servin Rathi[1], Inyeal Lee[1], Lijun Li[1], Muhammad Atif Khan[1], Dongsuk Lim[1], Yoontae Lee[1], Jinwoo Park[1], Anh Tuan Pham[3], Anh Tuan Duong[3], Sunglae Cho[3], Sun Jin Yun[4], and Gil-Ho Kim[1,*]

[1] *College of Information and Communication Engineering and Sungkyunkwan Advanced Institute of Nanotechnology (SAINT), Sungkyunkwan University, Suwon 16419, Korea*
[2] *Manufacturing Engineering Team, Memory Division, Samsung Electronics Co., Hwasung 18448, Korea*
[3] *Department of Physics and Energy Harvest-Storage Research Center, University of Ulsan, Ulsan 44610, Korea*
[4] *ICT Components and Materials Technology Research Division, Electronics and Telecommunications Research Institute, Daejeon 34129, Korea*

We demonstrate a high-performance photodetector with multilayer tin diselenide ($SnSe_2$) exfoliated from a high-quality crystal which was synthesized by the temperature gradient growth method. This $SnSe_2$ photodetector exhibits high photoresponsivity of 5.11×10^5 A W^{-1} and high specific detectivity of 2.79×10^{13} Jones under laser irradiation ($\lambda = 450$ nm). We also observed a reproducible and stable time-resolved photoresponse to the incident laser beam from this $SnSe_2$ photodetector, which can be used as a promising material for future optoelectronic applications.

Keywords: $SnSe_2$, Temperature Gradient Growth, Photodetector, Field Effect Transistor, Layered Chalcogenide Material.

1. INTRODUCTION

Two-dimensional (2D) layered chalcogenide materials (LCMs) have attracted enormous interests in wide research fields due to their unique physical and chemical properties. In particular, transition metal dichalcogenides and group III-VI/IV–VI LCMs are researched extensively for fundamental physical phenomena and various potential applications in electronics and optoelectronics due to their large specific surface area and tunable bandgaps.[1–6] As one of group IV–VI LCMs, tin diselenide ($SnSe_2$) is an earth abundant and low toxic *n*-type semiconductor with a hexagonal crystal structure of the CdI_2-type.[7–9] Moreover, it has been particularly studied in the fields of tunneling devices, field effect transistors, and photodetectors.[9–14] Similar to other LCMs, large area $SnSe_2$ films have been grown with various methods, such as chemical vapor deposition (CVD)[13,14] and molecular beam epitaxial[15] processes. Further, thin flakes of $SnSe_2$ could be obtained by mechanical exfoliation from bulk single-crystals synthesized by chemical vapor transport (CVT) method.[10,16] Since bulk crystals grown by CVT method can be easily contaminated by the transporting agent,[17] the melt growth methods, such as Czochralski and temperature gradient growth, have been improved to obtain pure and large bulk single-crystals.[18] The previous reported results on the $SnSe_2$ based optoelectronic devices use either flakes exfoliated from bulk single-crystal grown by CVT[16] method or films grown using CVD[13] process. In the present work, we studied the optoelectronic performance of $SnSe_2$ grown using the temperature gradient growth method, and report a high-performance photodetector fabricated using multilayer $SnSe_2$. This photodetector based on the exfoliated $SnSe_2$ flakes shows a maximum photoresponsivity of 5.11×10^5 A W^{-1} and a specific detectivity of 2.79×10^{13} Jones at a wavelength of 450 nm. These photoresponse properties are significantly higher than the previously reported results for $SnSe_2$ and comparable to the previously reported photodetectors based on other LCMs.

2. RESULTS AND DISCUSSION

The bulk $SnSe_2$ single-crystal used in this study were synthesized by the temperature gradient growth method.[18–21]

*Author to whom correspondence should be addressed.

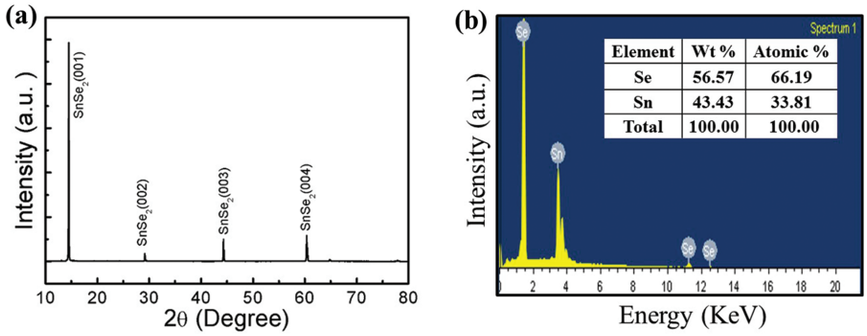

Figure 1. (a) The XRD data of the as-synthesized $SnSe_2$ crystal. (b) The EDX spectrum of the $SnSe_2$ crystal. The inset shows the atomic ratio of Sn and Se (∼1.96), which is close to the expected 1:2 stoichiometric composition of $SnSe_2$.

High Purity (99.999%) tin (Sn) and selenium (Se) powders were used for growing the bulk material. First, weighed powders of Sn and Se were loaded into a double-walled thick quartz ampoule and sealed in vacuum ($<10^{-4}$ Torr). Second, the sealed ampoule was loaded into a vertical furnace. Third, the temperature was slowly increased from room temperature to 750 °C and maintained for 10 hours. At last, the temperature was slowly cooled down to room temperature. In order to confirm the crystallinity and composition of the as-synthesized crystals, X-ray diffraction (XRD) and energy dispersive X-ray (EDX) analysis were performed. Figure 1(a) shows XRD data of the as-synthesized $SnSe_2$ crystal. The observed diffraction peaks match well with previously reported $SnSe_2$ powder XRD results and indicate that the $SnSe_2$ crystal has highly oriented layers with an interlayer distance of 0.614 nm.[6, 8–10] We further confirmed that the ratio of Sn and Se is approximately 1.96 by EDX analysis, which is close to the expected 1:2 stoichiometric composition of $SnSe_2$, as shown in Figure 1(b).

For fabricating $SnSe_2$ back-gated FET, the exfoliated $SnSe_2$ thin layers were placed onto a 285 nm-thick SiO_2 layer on a heavily doped *n*-type Si substrate. The source and drain electrodes were defined by photolithography, followed by Cr (10 nm)/Au (30 nm) metal deposition in an electron beam evaporation system and, subsequently, standard lift-off process was carried out with acetone. Figures 2(a) and (b) show a schematic illustration of $SnSe_2$ FET with electrical connections and an optical image of the $SnSe_2$ back-gated FET, respectively. The channel length (L) and width (W) are 5.09 μm and 5.02 μm, respectively. The inset in Figure 2(c) shows an atomic force microscopy (AFM) image. The thickness is measured to be 81.4 nm from the line-profile along the blue

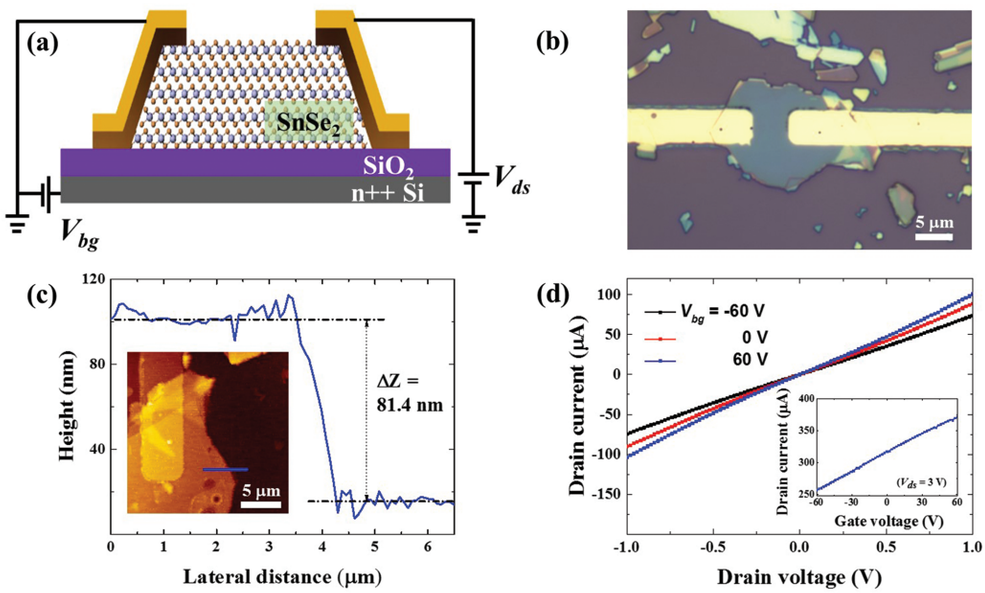

Figure 2. (a) Schematic illustration of $SnSe_2$ FET with electrical connections. (b) Optical image of $SnSe_2$ back-gated FET. The channel length and width are 5.09 μm and 5.02 μm, respectively. (c) AFM image (inset) and line-profile along the blue line on the $SnSe_2$ FET show a thickness of 81.4 nm. (d) Output characteristics with various V_{bg} at room temperature. The inset shows the transfer characteristic of the $SnSe_2$ FET in linear scale at $V_{ds} = 3$ V.

line on the $SnSe_2$ FET (Fig. 2(c)). We performed electrical characterization of the device in ambient and under dark using a Keithely 4200 semiconductor characterization system (4200-SCS). The output (I_{ds}–V_{ds}) and transfer (I_{ds}–V_{bg}) characteristics of the device are shown in Figure 2(d). The good linear relationship between the current and drain voltage indicates a good Ohmic contact between Cr/Au electrodes and $SnSe_2$. The multilayer $SnSe_2$ shows an *n*-type conduction behavior with a field effect mobility (μ_{FE}) about 28.44 $cm^2V^{-1}s^{-1}$, which is comparable to the previous reported $SnSe_2$ FETs.[9–11] However, the on/off current ratio is found to be only ∼1.23. This is because of the high electron density (∼10^{18} cm^{-3}) in $SnSe_2$ layer, which cannot be completely depleted by the back-gate induced electric field.[9, 10] The μ_{FE} was extracted using the equation $\mu_{FE} = (L/W) \times (g_m/C_{ox}V_{ds})$, where g_m is the transconductance, and C_{ox} is the dielectric capacitance between the channel and the back-gate per unit area. Here, we used the slope of the I_{ds}–V_{bg} curve to get the g_m, and C_{ox} is calculated using $C_{ox} = \varepsilon_0\varepsilon_r/d$, where ε_r is the relative permittivity of SiO_2, ε_0 is the free-space permittivity, and d is the SiO_2 thickness.

Raman scattering and photoluminescence (PL) characterizations were carried out to study the optical property of the $SnSe_2$ flakes. The characteristic peaks in the Raman spectrum, which was taken at room temperature using a 532 nm laser, as shown in Figure 3(a), confirm the flake as $SnSe_2$. The peak at 111.9 cm^{-1} corresponds to the E_g mode (in-plane vibration) and the intensity peak observed at 186.8 cm^{-1} is attributed to the A_{1g} mode (out-of-plane vibration) of $SnSe_2$.[9, 10, 16] Figure 3(b) shows PL spectrum of $SnSe_2$ FET (the same device measured in Fig. 2) using an excitation wavelength of 532 nm laser. The PL spectrum of $SnSe_2$ shows a sharp emission peak in the infrared region at 1074.7 nm (∼1.15 eV) almost corresponding to the band emission of $SnSe_2$ film.[21, 22] The Raman and PL analyses indicate the high quality of single-crystals of $SnSe_2$ synthesized by the temperature gradient growth method.

In the next step, we carried out optoelectrical characterization of the $SnSe_2$ photodetector in ambient condition. Figure 4(a) shows a schematic illustration of $SnSe_2$ photodetector under laser irradiation. Figure 4(b) shows the output characteristics of the 81.4 nm thick $SnSe_2$ photodetector (the same device measured in Fig. 2) under dark and laser irradiation with various effective incident power (P_{in}) at $\lambda = 450$ nm and $V_{bg} = -60$ V. Figure 4(c) shows photoresponsivity (R) and photocurrent (I_{ph}) of the $SnSe_2$ photodetector as a function of the P_{in} at $\lambda = 450$ nm, $V_{ds} = 3$ V, and $V_{bg} = -50$ V. R can be expressed as $R = I_{ph}/(P_{in}) = (I_{laser}–I_{dark})/(P_{in})$, where I_{laser} is the device current under laser irradiation and I_{dark} is the current measured in dark.[23, 24] It can be seen from the figure that R decreases from 5.11×10^5 to 2.75×10^4 A W^{-1} as the P_{in} increases from 0.096 to 9.643 nW. This decrease in R with P_{in} may be due to the existence of trap states in $SnSe_2$ or at the interface between $SnSe_2$ and SiO_2 layers.[5, 6] Specifically, the dependence of I_{ph} on P_{in} can be fitted by a simple power law: $I_{ph} = AP_{in}^{\alpha}$, where A is a scaling constant and α is an exponent.[21] The power equation fits (red line) to the experimental data (solid squares) with an exponent ($\alpha = 0.44$), and this nonlinear relationship suggests that a complex process related to the trap states caused by the defects or charge impurities present in $SnSe_2$ flake and the adsorbed molecules between $SnSe_2$ and SiO_2 interface.[13] Moreover, we calculated the specific detectivity (D^*), which is another performance index for photodetectors relevant to the sensitivity that a detector can distinguish from the background noise. Figure 4(d) shows the R and D^* of the $SnSe_2$ photodetectors as a function of P_{in} at $\lambda = 450$ nm, $V_{ds} = 3$ V, and $V_{bg} = -50$ V. By assuming that shot noise from dark current contributing to a major portion of the total noise, D^* is given by $D^* = RS^{1/2}/(2qI_{dark})^{1/2}$, where S is the active area of the photodetector and q is the unit of charge.[13, 24] The maximum R and D^* of $SnSe_2$ photodetector under laser irradiation ($\lambda = 450$ nm) were calculated to be 5.11×10^5 A W^{-1} and 2.79×10^{13} Jones, respectively. These results are higher than the previously reported results for $SnSe_2$ and comparable to the previously reported results based on LCMs.[25–27]

We further studied the effect of V_{bg} on I_{ph} in the $SnSe_2$ channel. Figure 5(a) shows the I_{ph} of the $SnSe_2$

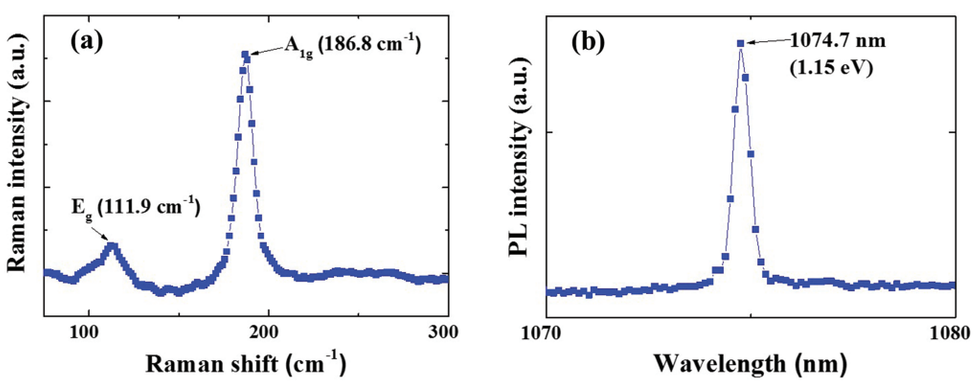

Figure 3. (a) Raman and (b) PL spectrum of $SnSe_2$ flakes, respectively. The Raman peak at 111.9 cm^{-1} corresponds to the E_g mode (in-plane vibration) and the intensity peak observed at 186.8 cm^{-1} is attributed to the A_{1g} mode (out-of-plane vibration) of $SnSe_2$.

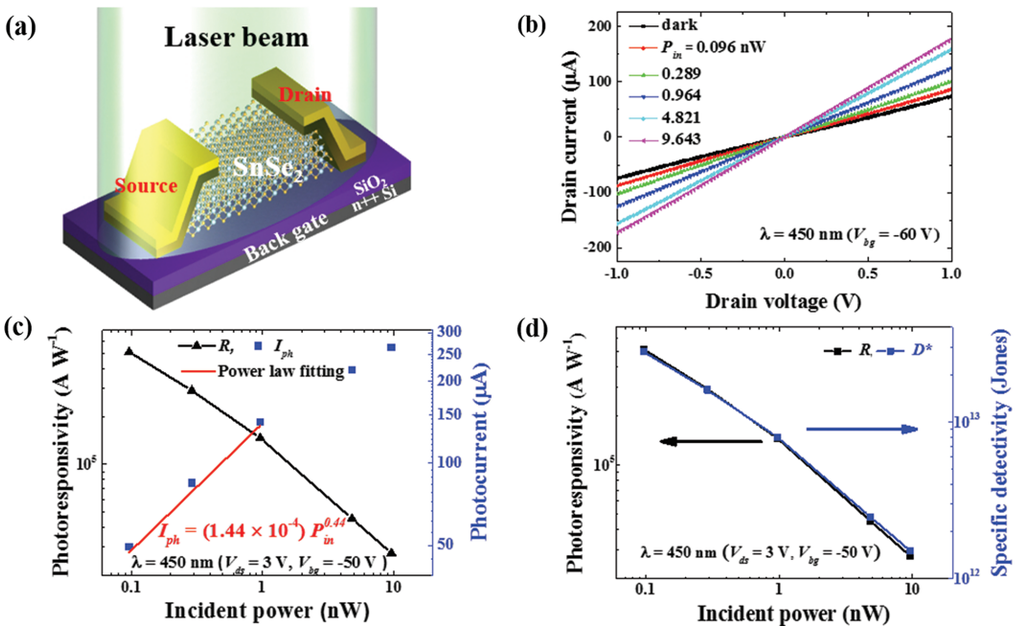

Figure 4. (a) Schematic illustration of $SnSe_2$ photodetector under laser irradiation. (b) Output characteristics of $SnSe_2$ photodetector under dark and laser irradiation with various P_{in} at $\lambda = 450$ nm and $V_{bg} = -60$ V. (c) The R and I_{ph} of $SnSe_2$ photodetector as a function of P_{in} at $\lambda = 450$ nm, $V_{ds} = 3$ V, and $V_{bg} = -50$ V. The red curve is fitted according to the power law $I_{ph} = AP_{in}^{\alpha}$: where A is a scaling constant and α is an exponent. (d) The R and D^* of $SnSe_2$ photodetector as a function of P_{in} at $\lambda = 450$ nm, $V_{ds} = 3$ V, and $V_{bg} = -50$ V.

photodetector as a function of the P_{in} at $\lambda = 450$ nm, $V_{ds} = 3$ V, and $V_{bg} = -50$ to $+60$ V. As the V_{bg} increases from -50 to 60 V, the exponent of fitting curve, increases from 0.44 to 0.5. Figure 5(b) shows the R and D^* of the $SnSe_2$ photodetector as a function of V_{bg} with a fixed P_{in} (=0.964 nW) at $\lambda = 450$ nm and $V_{ds} = 3$ V. In the range of V_{bg} from -50 to 60 V, the photoresponsivity was varied from 1.46×10^5 to 1.25×10^5. These variations with

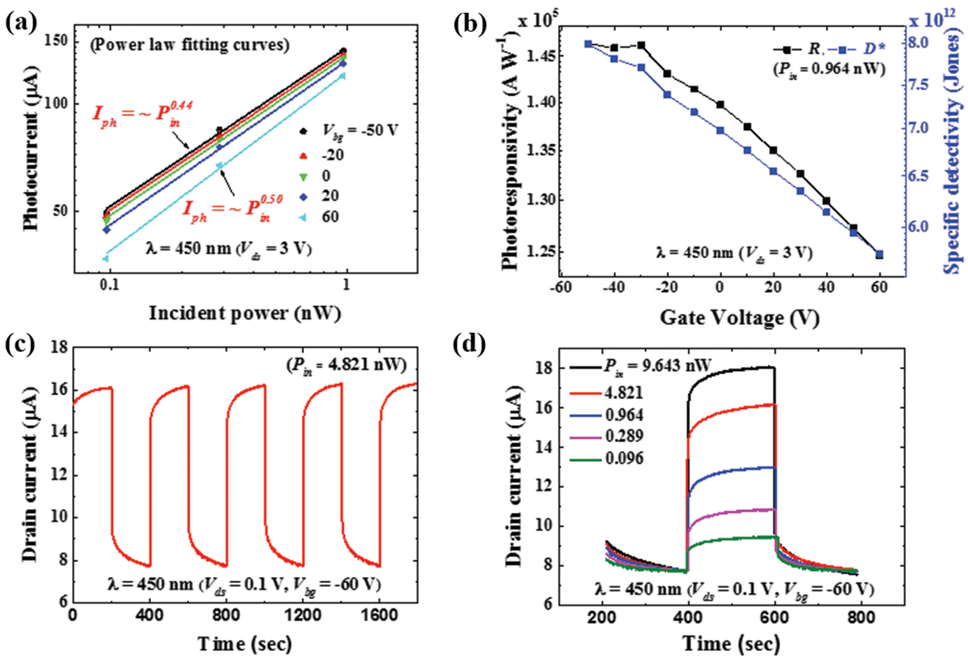

Figure 5. (a) The I_{ph} of $SnSe_2$ photodetector as a function of P_{in} at $\lambda = 450$ nm, $V_{ds} = 3$ V, and $V_{bg} = -50$ to $+60$ V. The curves are fitted according to the power law $I_{ph} = AP_{in}^{\alpha}$, respectively. (b) The R and D^* of $SnSe_2$ photodetector as a function of V_{bg} with a fixed P_{in} (=0.964 nW) at $\lambda = 450$ nm and $V_{ds} = 3$ V. (c) The time-resolved photoresponse of the $SnSe_2$ photodetector with a fixed P_{in} (=4.821 nW) at $\lambda = 450$ nm, $V_{ds} = 0.1$ V, and $V_{bg} = -60$ V. (d) The time-resolved photoresponse of the device with various P_{in} at $\lambda = 450$ nm, $V_{ds} = 0.1$ V, and $V_{bg} = -60$ V.

back gate can be explained from the complex behavior of recombination and generation thorough traps and impurities states both in the material and at the interface. Further, the higher charge carrier density, with the increase in the gate voltage results in higher carrier scattering in the channel which lowers the mobility and increases the recombination probability of the photoexcited carriers, leading to the decrease of photoresponsivity.[28] These results show that we can optimize the photodetector characteristics, such as I_{ph}, R, and D^*, by applying an optimized V_{bg}. Figures 5(c) and (d) show the time-resolved photoresponse of the device with a fixed P_{in} ($= 4.821$ nW) and various P_{in}, respectively, at $\lambda = 450$ nm, $V_{ds} = 0.1$ V, and $V_{bg} = -60$ V. The $SnSe_2$ photodetector exhibits a repeatable and stable response to the incident laser beam as shown in Figure 5(c), with laser irradiation ($\lambda = 450$ nm) for more than 30 minutes. Figure 5(d) also shows a clear time-resolved photoresponse under various P_{in}. Such reproducible response, even at a very low P_{in} ($= 0.096$ nW) and switching stability are important characteristics for photodetector operation.

3. CONCLUSION

In conclusion, we have demonstrated a high-performance photodetector with multilayer $SnSe_2$ exfoliated from a high-quality crystal which was synthesized by the temperature gradient growth method. We obtained photoresponsivity of 5.11×10^5 A W^{-1} and specific detectivity of 2.79×10^{13} Jones at the wavelength of 450 nm, these values are higher than or comparable to the reported values of other individual LCMs based photodetectors. This $SnSe_2$ photodetector also shows a clear photoresponse even at a very low laser irradiation power of 0.096 nW. Our study suggests that multilayer $SnSe_2$ with high photoresponsivity can be used as a promising material for future optoelectronic applications.

Acknowledgments: This research was supported by the Basic Science Research Program through the National Research Foundation of Korea (NRF) funded by the Ministry of Education, Science and Technology (Nos. 2016R1A2A2A05921925 and 2016R1D1A1B03932455) and Korea Research Fellowship Program through the NRF funded by the Ministry of Science, ICT and Future Planning (NRF-2015H1D3A1062519). This work was partly supported by Institute for Information and Communications Technology Promotion (IITP) grant funded by the Korea government (MSIP) (B0117-16-1003, Fundamental technologies of two-dimensional materials and devices for the platform of new-functional smart devices).

References and Notes

1. G. R. Bhimanapati, Z. Lin, V. Meunier, Y. Jung, J. Cha, S. Das, D. Xiao, Y. Son, M. S. Strano, V. R. Cooper, L. Liang, S. G. Louie, E. Ringe, W. Zhou, S. S. Kim, R. R. Naik, B. G. Sumpter, H. Terrones, F. Xia, Y. Wang, J. Zhu, D. Akinwande, N. Alem, J. A. Schuller, R. E. Schaak, M. Terrones, and J. A. Robinson, *ACS Nano* 9, 11509 (**2015**).
2. M. Kang, S. Rathi, I. Lee, D. Lim, J. Wang, L. Li, M. A. Khan, and G.-H. Kim, *Appl. Phys. Lett.* 106, 143108 (**2015**).
3. S. Rathi, I. Lee, D. Lim, J. Wang, Y. Ochiai, N. Aoki, K. Watanabe, T. Taniguchi, G.-H. Lee, Y.-J. Yu, P. Kim, and G.-H. Kim, *Nano Lett.* 15, 5017 (**2015**).
4. W. Feng, J.-B. Wu, X. Li, W. Zheng, X. Zhou, K. Xiao, W. Cao, B. Yang, J.-C. Idrobo, L. Basile, W. Tian, P. Tan, and P. Hu, *J. Mater. Chem. C* 3, 7022 (**2015**).
5. X. Zhou, Q. Zhang, L. Gan, H. Li, and T. Zhai, *Adv. Funct. Mater.* 26, 4405 (**2016**).
6. R. K. Ulaganathan, Y.-Y. Lu, C.-J. Kuo, S. R. Tamalampudi, R. Sankar, K. M. Boopathi, A. Anand, K. Yadav, R. J. Mathew, C.-R. Liu, F. C. Chou, and Y.-T. Chen, *Nanoscale* 8, 2284 (**2016**).
7. Z. Fang, S. Hao, L. Long, H. Fang, T. Qiang, and Y. Song, *Cryst. Eng. Comm.* 16, 2404 (**2014**).
8. S. Saha, A. Banik, and K. Biswas, *Chem. Eur. J.* 22, 15634 (**2016**).
9. T. Pei, L. Bao, G. Wang, R. Ma, H. Yang, J. Li, C. Gu, S. Pantelides, S. Du, and H.-J. Gao, *Appl. Phys. Lett.* 108, 053506 (**2016**).
10. C. Guo, Z. Tian, Y. Xiao, Q. Mi, and J. Xue, *Appl. Phys. Lett.* 109, 203104 (**2016**).
11. Y. Su, M. A. Ebrish, E. J. Olson, and S. J. Koester, *Appl. Phys. Lett.* 103, 263104 (**2013**).
12. T. Roy, M. Tosun, M. Hettick, G. H. Ahn, C. Hu, and A. Javey, *Appl. Phys. Lett.* 108, 083111 (**2016**).
13. X. Zhou, L. Gan, W. Tian, Q. Zhang, S. Jin, H. Li, Y. Bando, D. Golberg, and T. Zhai, *Adv. Mater.* 27, 8035 (**2015**).
14. Y. Huang, K. Xu, Z. Wang, T. A. Shifa, Q. Wang, F. Wang, C. Jiang, and J. He, *Nanoscale* 7, 17375 (**2015**).
15. K. E. Aretouli, D. Tsoutsou, P. Tsipas, J. Marquez-Velasco, S. A. Giamini, N. Kelaidis, V. Psycharis, and A. Dimoulas, *ACS Appl. Mater. Interfaces* 8, 23222 (**2016**).
16. P. Yu, X. Yu, W. Lu, H. Lin, L. Sun, K. Du, F. Liu, W. Fu, Q. Zeng, Z. Shen, C. Jin, Q. J. Wang, and Z. Liu, *Adv. Funct. Mater.* 26, 137 (**2016**).
17. M. K. Agarwal, P. D. Patel, and S. S. Patel, *J. Cryst. Growth* 110, 553 (**1991**).
18. H. Jiang and C. Kloc, *MRS Bull.* 38, 28 (**2013**).
19. S.-U. Kim, A.-T. Duong, S. Cho, S. H. Rhim, and J. Kim, *Surf. Sci.* 651, 5 (**2016**).
20. E. Trifonova, I. Y. Yanchev, P. Manou, K. Kambas, and A. N. Anagnostopoulos, *J. Mater. Sci.* 31, 3647 (**1996**).
21. C. Julien, M. Eddrief, I. Samaras, and M. Balkanski, *Mater. Sci. and Eng. B* 15, 70 (**1992**).
22. E. Barrios-Salgado, M. T. S. Nair, and P. K. Nair, *Thin Solid Films* 598, 149 (**2016**).
23. I. Lee, S. Rathi, D. Lim, L. Li, J. Park, Y. Lee, K. S. Yi, K. P. Dhakal, J. Kim, C. Lee, G.-H. Lee, Y. D. Kim, J. Hone, S. J. Yun, D.-H. Youn, and G.-H. Kim, *Adv. Mater.* 28, 95169 (**2016**).
24. H. Huang, J. Wang, W. Hu, L. Liao, P. Wang, X. Wang, F. Gong, Y. Chen, G. Wu, W. Luo, H. Shen, T. Lin, J. Sun, X. Meng, X. Chen, and J. Chu, *Nanotecnology* 27, 445201 (**2016**).
25. E. Liu, M. Long, J. Zeng, W. Luo, Y. Wang, Y. Pan, W. Zhou, B. Wang, W. Hu, Z. Ni, Y. You, X. Zhang, S. Qin, Y. Shi, K. Watanabe, T. Taniguchi, H. Yuan, H. Y. Hwang, Y. Cui, F. Miao, and D. Xing, *Adv. Funct. Mater.* 26, 1938 (**2016**).
26. M. Huang, M. Wang, C. Chen, Z. Ma, X. Li, J. Han, and Y. Wu, *Adv. Mater.* 28, 3481 (**2016**).
27. G. Konstantatos, M. Badioli, L. Gaudreau, J. Osmond, M. Bernechea, F. P. G. de Arquer, F. Gatti, and F. H. L. Koppens, *Nat. Nanotechnol.* 7, 363 (**2012**).
28. W. Zhang, J.-K. Huang, C.-H. Chen, Y.-H. Chang, Y.-J. Cheng, and L.-J. Li, *Adv. Mater.* 25, 3456 (**2013**).

Received: 9 December 2016. Accepted: 3 June 2017.